

Northumbria Research Link

Citation: Saeed, Huzaifa, Maqsood, Adnan, Dala, Laurent and Sherbaz, Salma (2022) Numerical Investigation of Aerodynamic and Stability Behavior of Corrugated Airfoils at Low Reynolds Number. In: AIAA SCITECH 2022 Forum. American Institute of Aeronautics and Astronautics, Reston, US, 0704. ISBN 9781624106316

Published by: American Institute of Aeronautics and Astronautics

URL: <https://doi.org/10.2514/6.2022-0704> <<https://doi.org/10.2514/6.2022-0704>>

This version was downloaded from Northumbria Research Link:
<https://nrl.northumbria.ac.uk/id/eprint/48185/>

Northumbria University has developed Northumbria Research Link (NRL) to enable users to access the University's research output. Copyright © and moral rights for items on NRL are retained by the individual author(s) and/or other copyright owners. Single copies of full items can be reproduced, displayed or performed, and given to third parties in any format or medium for personal research or study, educational, or not-for-profit purposes without prior permission or charge, provided the authors, title and full bibliographic details are given, as well as a hyperlink and/or URL to the original metadata page. The content must not be changed in any way. Full items must not be sold commercially in any format or medium without formal permission of the copyright holder. The full policy is available online: <http://nrl.northumbria.ac.uk/policies.html>

This document may differ from the final, published version of the research and has been made available online in accordance with publisher policies. To read and/or cite from the published version of the research, please visit the publisher's website (a subscription may be required.)

Numerical Investigation of Aerodynamic and Stability Behavior of Corrugated Airfoils at Low Reynolds Number

Huzaifa Saeed* and Adnan Maqsood†

National University of Sciences & Technology, Islamabad, 44000, Pakistan.

Laurent Dala‡

Northumbria University, Newcastle upon Tyne, NE1 8ST, United Kingdom.

Salma Sherbaz§

National University of Sciences & Technology, Islamabad, 44000, Pakistan.

A comprehensive computational study of the aerodynamic performance and stability characteristics of corrugated airfoils has been conducted at the Low-Reynolds number corresponding to the flight regime of micro-aerial vehicles (MAVs). This research aims to explore the applicability of bio-inspired airfoils in the design of MAVs and to study the effect of corrugations, and thus the entrapped vortices on the inherent tendency of airfoils to diminish flight disturbances. Computational fluid dynamics (CFD) analyses have been performed on three dragonfly-based corrugated airfoils, flat plate, and a "smoothened version" of a pleated airfoil; a comparison of their aerodynamic coefficients is discussed. The stability aspect of these airfoils is studied by estimating dynamic longitudinal damping coefficients at different angles of attack. These damping coefficients are calculated by inducing forced sinusoidal oscillations centered at the quarter-chord of each airfoil while maintaining the reduced frequency (k) in a quasi-steady aerodynamic regime. The interlink relation of the time-step size of transient simulations with the angular frequency of oscillations is also discussed concisely. The aerodynamic results show little-to-no difference between the pleated and smoothened version of the airfoil; thus, further strengthening the notion of the existence of a "switch-over" region from pleated airfoil to smoothened airfoil near Reynolds number (Re) of 100,000. Similarly, the perusal of dynamic damping coefficients of airfoils also suggests a negligible effect of corrugations or entrapped vortices on the stability behavior of airfoil.

I. Nomenclature

b	=	semi-chord length i.e., chord length/2, m
c	=	chord
C_l	=	lift coefficient
C_d	=	drag coefficient
C_m	=	pitching moment coefficient
C_{m0}	=	coefficient of pitching moment at 0° angle of attack
$C_{m\alpha}$	=	coefficient of pitch moment derivative due to change in angle of attack
C_{mq}	=	coefficient of dynamic stability derivative (or pitch damping coefficient) due to pitch rate
$C_{m\dot{\alpha}}$	=	coefficient of dynamic stability derivative due to the rate of change of angle of attack
K	=	reduced frequency
q	=	pitch rate
\bar{q}	=	nondimensionalized pitch rate
Re	=	Reynolds number
t	=	time, s

*Graduate Student, Research Centre for Modeling and Simulation

†Associate Professor, Research Centre for Modeling and Simulation.

‡Professor, Department of Mechanical and Construction Engineering.

§Assistant Professor, Research Centre for Modeling and Simulation.

V_∞	=	freestream velocity
α	=	angle of attack, deg
$\dot{\alpha}$	=	time rate of change of angle of attack, deg/s
$\bar{\alpha}$	=	non-dimensionalized time rate of change of angle of attack
ω	=	angular velocity of airfoil, rad . s ⁻¹

II. Introduction

DURING the last few decades, a significant amount of research has been invested in developing unmanned aerial vehicles (UAVs). These are small flying aircraft that can perform a variety of missions at any instant of time, such as aerial surveillance, remote sensing, search, and rescue tasks in challenging environments. Also, they are cost-effective in performing their mission and pose a minimum human risk due to the absence of an active pilot [1]. Instead, the aircraft is remotely controlled by a pilot from the ground station unit (GSU), or it performs its mission using pre-mission data. Though being operated autonomously or remotely controlled, UAVs have proved their capability to accomplish their missions with utmost accuracy [1].

As days pass by, the role of UAVs does not remain restricted to reconnaissance missions. Still, it is expanding into new horizons: Local delivery methods are now seen to be evolving from the conventional traffic vehicle to autonomous air vehicles as certain food business enterprises have started delivering food and grocery items via UAVs [2]. In this way, they managed to cut down a significant amount of cost and provide the commodities timely, without affecting the traffic situation. Furthermore, during the COVID-19 pandemic, UAVs have been used to carry out disinfection activities on a massive scale [3, 4]. From the previously mentioned fact, it is evident that UAVs will play an essential role in shaping our lives soon.

Micro aerial vehicles (MAVs) are a miniature version of UAVs that can easily be deployed in numbers, and their flight cost is less than conventional alternatives. Moreover, they can perform their mission in an immediate and urban environment like inside tunnels, shafts, buildings, etc.[1]. These features have captivated the interest of researchers, and much of the work is underway to attain their flight [5]. Based on their mission profile, specific guidelines and performance requirement for the design of MAVs have been established. Pines and Bohorquez provided the design MAV requirement for a typical MAV with a mass around 100 g, and the maximum dimension should not be more than 15.24 cm [1]. As the mission profile of MAVs suggests that their flight remains in sea-level conditions, it can be inferred that MAVs encounter a low Reynolds number of around 100,000. The flow at this Reynolds number is dominated by viscous effects [6].

The aerodynamic characteristic of airfoils is greatly dependent on Reynolds number. For conventional airfoil, the aerodynamic performance is reduced with the decrease in Reynolds number, which can be observed from the lower lift coefficient values and higher drag coefficient values [6, 7]. Low Reynolds number flows also give rise to phenomena like separation bubbles and early stall. The separation bubble is a slow reverse-flow vortex region that induces turbulence in the flow, is formed when the flow detaches from the portion of the surface before reattaching downstream. This happens due to the low Reynolds number flow's inherent poor capability to withstand against adverse pressure gradient, as the flow has low kinetic energy to overcome the pressure gradient and shear effects. Furthermore, the separation bubble grows with the increase in the angle of attack (AoA) and moves towards the leading edge, and thus eventually 'burst', resulting in an early stall. Stall angle is reduced because of the phenomenon, and there is a drastic increase in drag, thus affecting the whole aerodynamic performance of the airfoil [8].

At the ultra-low Reynolds number (Re 10 10,000), nature opts for corrugated airfoils over conventional. This can be verified by observing the wing section of insects and small birds [9]. Their protruding surface at the leading edge causes an early transition from laminar to turbulent flow. Furthermore, the corrugation over the airfoil generates entrapped vortex regions that rotate clockwise before stall and act as 'turbulators' by transferring the portion of their turbulent kinetic energy (TKE) to the flow above. This transferring of TKE and clockwise rotation of vortex cause the flow to remain near the surface and follow a smooth streamline envelop; thus, effectively delaying the stall. However, Tamai and Hui observed that in the post-stall regime, the direction of the vortex is reversed, resulting in more separation as compared to the conventional airfoil, and thus drag increased eventually [8]. Murphy performed particle image velocimetry (PIV) based experiments over both pleated and smooth airfoil at different Reynolds numbers and found out that the aerodynamic performance of pleated airfoils was higher at a low Reynolds number. But at Re 125,000 and above, smooth airfoil superseded the pleated airfoils. Murphy suggested a switchover in performance from pleated to smooth airfoil, which occurs around Re 100,000 [10].

The typical flight of MAVs is around Re 100,000 according to the MAV design specification [1, 11]. Although a

significant amount of investigation and experimentation have been performed upon the study of flow over corrugated airfoils and their aerodynamic performance at low Re, yet there is a less amount of research available on another aspect of flight, i.e., the effect of corrugations on the inherent response of the airfoil experiencing disturbance. Stability coefficients define the air vehicle's response to external or internal disturbances and play a crucial role in designing an aircraft and must also be studied for desirable control design that will ensure safe flight [12].

MAVs' flight-envelop is not insusceptible of turbulence, and due to its geometrical and weight constraints, a small gust of wind could have a considerable impact on its flight. These flight disturbances need to be rejected over time either by the aircraft's inherent tendency or by applying appropriate control surface.

This research is focused on studying the effect of the entrapped vortices on the intrinsic disturbance rejection capability of the geometry over time. The study of the impact of corrugations on the airfoil on the overall stability, precisely the dynamic stability of the airfoil, is currently limited. This paper aims to numerically investigate and compare the effect of these corrugations on the aerodynamic and stability characteristics at low Re numbers. For this purpose, five airfoils have been studied: three pleated airfoils, one smoothed airfoil generated by combining the extrema of a pleated airfoil and a flat plate. These investigations were carried out at a Re number of 100,000 mainly due to two reasons: the typical flight regime of MAVs and comparing the airfoils at switchover Re number, i.e., when their aerodynamic performance is quite similar. Also, the aerodynamic performance of pleated airfoils remains almost unchanged with the change of Reynolds number as identified by Ellington and Murphy [9, 10].

ANSYS FLUENT is a high-fidelity software capable of handling a large variety of complex flows with an appreciable amount of accuracy. For this reason, the investigations were carried out on ANSYS FLUENT 17.

III. CFD Model

A. Geometry Generation

In this numerical study, five airfoils of different characteristics are studied. Out of five, three were corrugated airfoils, a flat plate, and a smoothed airfoil. The geometrical description of these airfoils is given below.

A flat plate airfoil based on the experimental research by Torres and Mueller was generated. It is a 5-to-1 elliptical leading-edge airfoil having a thickness-to-chord ratio of 1.96%, which is the same as used by Cosyn and Vierendeels [13] as shown in Fig. 1 [13–15].

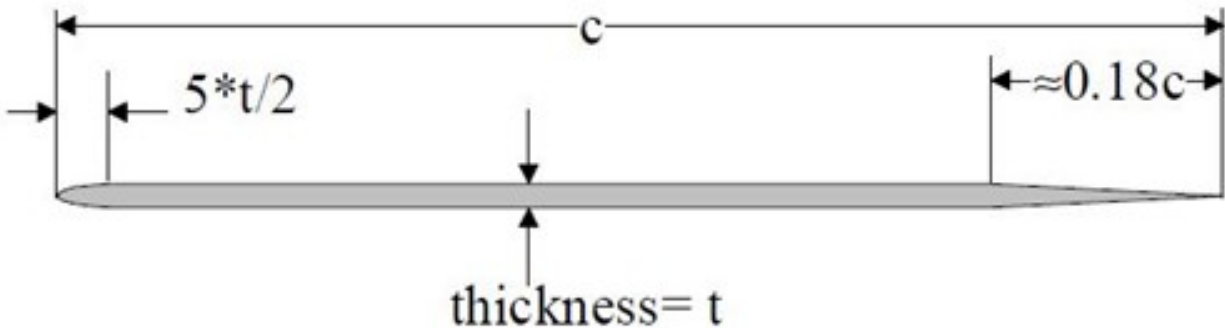


Fig. 1 Flat Plate.

Moreover, Kesel provided the profiles of pleated airfoils corresponding to different wing sections of a dragonfly [16]. Data points in the form of cartesian coordinates of two of Kesel's airfoils, Profile 1 and Profile 3, were carefully extracted using Plot Digitizer, a Java-based program to extract data from the given scanned documents digitally. These data points were then exported to ANSYS DesignModeler for geometry generation. A smoothed version of Profile 3 was also generated by joining the extrema of the corrugations, as set out by Kesel and is referred to as Profile 3A. The terminology of these three airfoils is the same as used by Kesel for ease in referencing.

Furthermore, Murphy generated a corrugated airfoil which was based on Kesel's Profile 2. Though the profile was similar in terms of corrugations and overall shape, it differs in thickness. Since Murphy performed PIV experiments at Re 100,000 on this airfoil and provided coordinates of the airfoils and the experimental results, this profile was studied because the flow conditions were more pertinent with this research [10]. This also provided another CFD validation case

based on corrugated airfoil aside from the flat plate experimental studies done by Torres and Mueller and the numerical investigation done by Cosyn. Again, Kesel's nomenclature was maintained, and this profile is referred to as Profile 2 in this research. The chord length has been kept the same as Kesel, Murphy, or Torres provided to preserve the aspect ratio. The velocity is varied to simulate the Reynolds number of 100,000. A comparison of all these airfoils to the original airfoils can be seen in Fig. 2 and Fig. 3.

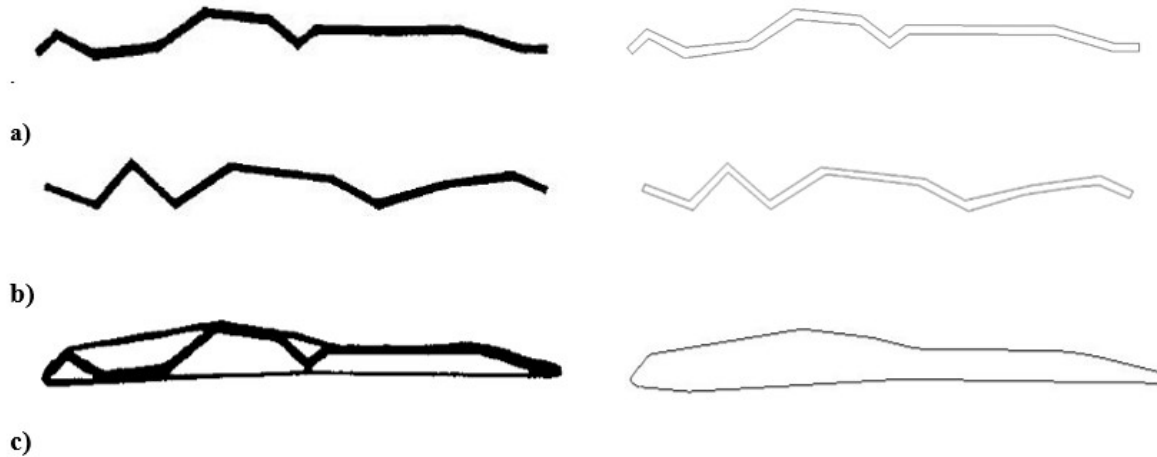


Fig. 2 Profiles Kesel (Left) and corresponding generated airfoils; a) Profile 1 b) Profile 3 c) Profile 3A.



Fig. 3 Profile 2 from Murphy (left) and corresponding digitally generated airfoil.

B. CFD Setup

Two dimensional CFD pressure-based coupled solver is generated. Spalart-Allmaras turbulence model is used whereas Courant number of 200 is set and density is kept constant in all simulations due to incompressible properties of air at low velocities. The velocity inlet boundary condition specifies incoming flow, whereas the pressure outlet is chosen for the outlet condition. Flow variables have been discretized using the second-order upwind scheme, and a second-order implicit method is employed for transient formulations. Time step size is selected while keeping the effect of amplitude and frequency of oscillations in consideration. Discussions on the selection of grid size, turbulence model, discretization scheme, and time step size selection are provided in the later sections. Numerical results show a good agreement with experimental and other CFD-established results.

C. CFD Model Selection

The effect of domain size has been checked by generating three rectangular domains of different sizes on a 5-to-1 elliptical leading edge flat plate airfoil based on Muller [14, 15, 17]. The names of the domains are referred to as Domain 1, Domain 2, and Domain 3, with Domain 1 being the smallest and Domain 3 as the largest. The sizes of these domains are given in Table 1. After performing mesh sensitivity analysis in each domain with respect to aerodynamic coefficients, Domain 2 of size $18c \times 14c$, where 'c' is referred to as chord length, is selected for further analyses. The mesh sensitivity of this domain was achieved around 450,000 elements. Furthermore, it can also be seen in Fig. 4 that the domain is insensitive concerning aerodynamic coefficient at the pertinent range of angles of attack.

In addition, the mesh near the airfoils is also kept dense, and a y^+ value of less than one is maintained throughout the chord length of all studied airfoil for better boundary layer resolution. The final mesh near the airfoil 'Profile 3A' is shown in Fig. 5, and all the other meshes were similar. The total computational time for steady CFD calculation was about 3 hours for a single simulation. It took approximately 36 hours to calculate dynamic stability coefficients at a single angle of attack. The computations were carried out on six computing nodes: each node having 8 Intel E5520 CPUs. In total, around 150 CFD simulations were carried out.

Table 1 Mesh Domain Sizes

Domain Name	Sizes as multiple of chord length Length x Height
Domain 1	$10c \times 8c$
Domain 2	$18c \times 14c$
Domain 3	$27c \times 18c$

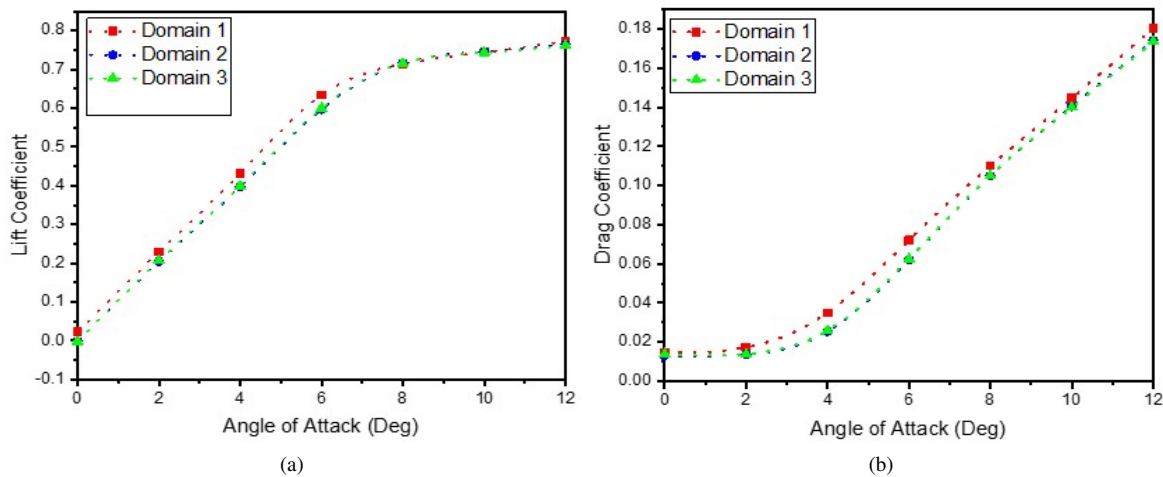


Fig. 4 C_l and C_d of a two-dimensional flat plate at different sizes of domain, Re 100,000.

A circular region of radius 1.5 times the chord length, centered at the mid-chord of the airfoil, is also generated to create a rotating region in simulations to extract pitching dynamic stability derivatives. For the mesh and CFD model validation, simulations based on appropriate RANS-based turbulence models have been carried out on a flat plate. It has been found that the Spalart-Allmaras model shows better agreement with the experiment results and established numerical results, depicted in Fig. 6. Cosyn also observed the superiority of Spalart-Allmaras at Re 100,000 due to its better capability to obtain good results for properly resolved boundary layers under an adverse pressure gradient. Especially at higher angles of attack, Spalart-Allmaras is seen to outperform all the other models by a significant margin, as results were closer to Mueller's experiment than Cosyn's numerical results [13, 15].

The deviation from the experimental results at small angles of attack is due to the formation of a separation bubble, as explained by Cosyn. Since no transition model is used, this separation bubble is not captured appreciably by the Spalart-Allmaras turbulence model, which is reflected in the results. Yet, considering computational cost and desired accuracy, Cosyn found that Spalart-Allmaras is the most suitable turbulence model. Thus, this turbulence model is selected for further investigation in this research [13].

The confidence in this CFD model is further strengthened by performing additional validation using a corrugated airfoil instead of a smooth airfoil. Murphy performed particle image velocimetry (PIV) measurements over a corrugated airfoil (similar to Kesel's [16] dragonfly airfoil 'Profile 2') and compared its aerodynamic behavior with streamlined airfoil and flat plate. For this CFD validation study, CFD simulations were carried out over the geometry provided by Murphy. The results are within 15% error, as can be seen from Fig. 7. The coefficient of lift is well within the range except at small angles of attack (AoA), which is again due to the phenomenon of separation bubble explained

earlier. Although there is a disparity between the results at high angles of attack, it can be ignored as dynamic stability coefficients are calculated up to 6° angles of attack.

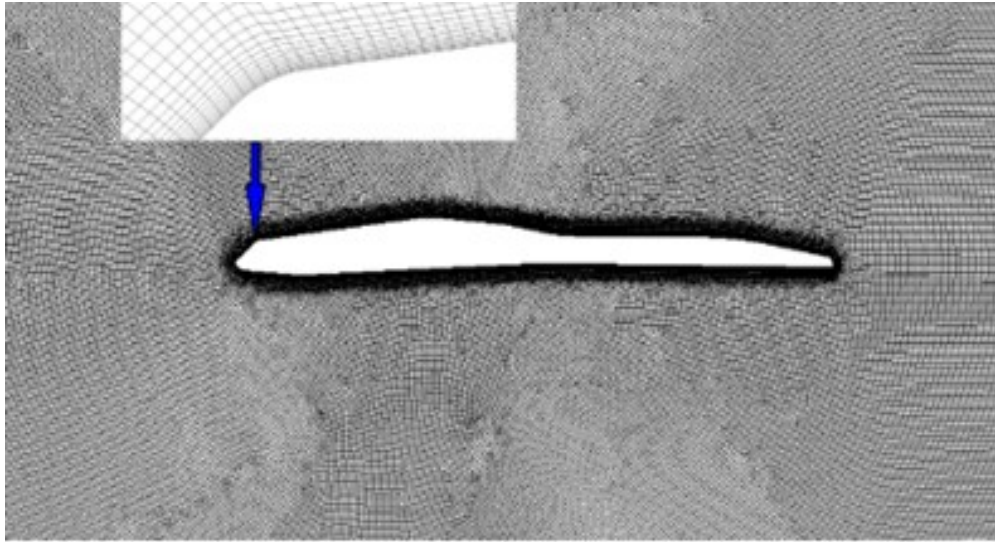


Fig. 5 Close-up view of mesh around Profile 3A.

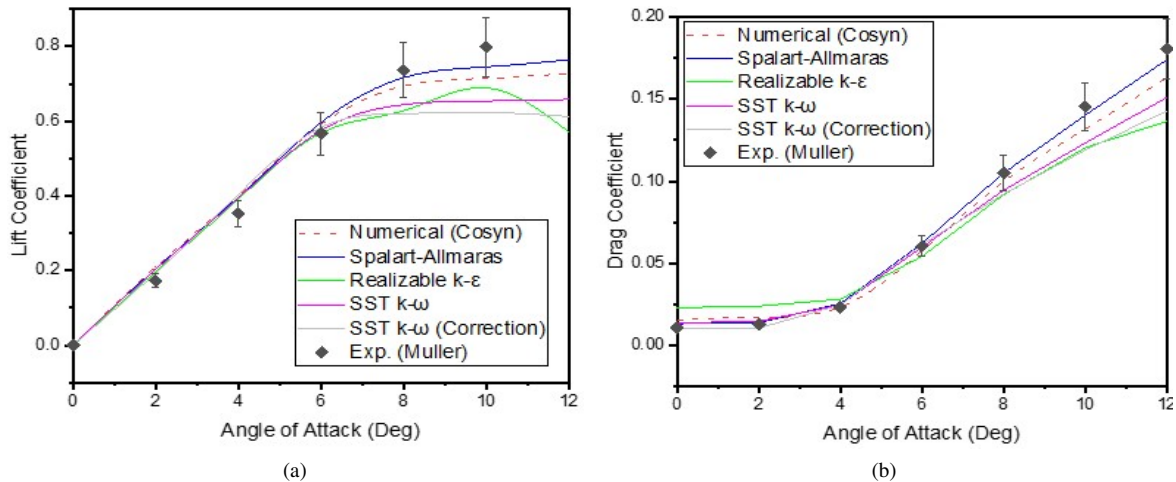


Fig. 6 Comparison of different turbulence models, $Re\ 100,000$.

D. Numerical Results

A tight numerical convergence criterion is selected for both steady and transient simulations while considering the computational cost. For calculating aerodynamic coefficients, results are considered to be numerically converged when all the residuals are below 1×10^{-1} . Similarly, the convergence criteria for transient simulations are set at 5×10^{-7} for each time step. In transient CFD simulations, the solution achieves convergence in an average of 40 iterations/time step.

Steady-state CFD simulations are performed at angles of attack ranging from $0 - 12^\circ$ angle of attack. Lift, drag, and moment coefficients are calculated for each airfoil and presented in Fig. 8, Fig. 9 and Fig. 10. The graph also indicates stall angles for these airfoils, which can also be observed from the streamlines and velocity contours shown in Fig. 11. This information is essential as calculating dynamic stability derivatives at near and post-stall angles requires a more rigorous CFD model and is more prone to erroneous results. Consequently, the calculation of dynamic stability

derivatives is restricted to pre-stall angles of attack in this research. The aerodynamic performance of the airfoils is discussed below.

1. Flat Plate

Although the lift coefficient and maximum lift coefficient of the flat plate are not as impressive as other airfoils, it displays the lowest drag among all the studied airfoils at low angles of attack. However, a substantial rise in the drag coefficient is seen as the angle of attack is increased. This could be because of the low kinetic energy available at Re 100,000 and the absence of a circulating region near the wall that otherwise could have energized the flow. Due to the symmetrical nature of the airfoil, the moment coefficient at the quarter chord is observed to be nearly equal to zero at pre-stall angles of attack. This observation is in line with the "thin flat plate theory." Since the theory does not account for the post-stall effect and assumes zero drag, the quarter-chord moment coefficient at high angles of attack is not seen to be at zero, as pressure distribution is disturbed at high angles of attack. Moreover, there is also an appreciable amount of drag present at higher angles of attack. This could be seen from the streamlines calculated at a stall angle of 8° , as shown in Fig. 11, where the formation of a sizeable circulating separation bubble can be seen, and the flow is fully separated from the surface.

2. Profile 1

Profile 1 exhibits a lift coefficient similar to the flat plate except at high angles of attack where it achieves higher C_l and $C_{l, \max}$. However, the drag coefficient is much higher for Profile 1 and other corrugated airfoils than flat plate or smoothed airfoil (Profile 3A) because of two reasons. First, the distance covered by the fluid while moving from the leading edge to the trailing edge is more in corrugated airfoils due to protrusions. This increased distance intensifies the skin friction drag for corrugated airfoils. Second, a small reverse vortex region is created in the 'valley' region and near the surface of the pleated airfoils at the near stall and post-stall angles of attack. This reverse vortex region is anticlockwise in the upper and clockwise in the lower surface, thus aiding flow separation. As mentioned by Murphy [10], this phenomenon is observed in the numerical simulations of all the corrugated airfoils at higher angles of attack in Fig. 12.

Moreover, from Fig. 10, Profile 1 shows a negative moment coefficient at 0° angle of attack, i.e., it has negative values of ' c_{m0} ', which reflects the aircraft's ability to trim at either positive or negative angles of attack depending on the positive or negative values of ' c_{m0} ' respectively. In most cases, it is desirable for air vehicles to be able to trim at positive angles of attack, i.e., the positive value of ' c_{m0} '. Also, the moment coefficient of Profile 1 shows an increasing trend with the angles of attack in Fig. 10. This infers the positive value of ' $c_{m\alpha}$ ' suggesting the airfoil is statically unstable.

3. Profile 2

In terms of the coefficient of lift, Profile 2 was somewhat lying between flat plate and Profile 3 at pre-stall angles. However, it suffered an early stall and a lower value of $C_{l, \max}$. Furthermore, the drag coefficient was also found to be very high, in fact, highest among all the other airfoils at post-stall angles of attack. This can be seen from Fig. 8 and Fig. 9 that as stall occurs, there is a rapid rise in the drag coefficient. Thus, it can be inferred that the stall penalty is highest for Profile 2 at Reynolds number 100,000, which may be due to the airfoil's thicker profile compared to others, and thus resulting in a more significant separation bubble region as shown in Fig. 11. Finally, by looking at the values of the moment coefficient, it can be observed that the airfoil possesses positive values of ' c_{m0} ' at all angles of attack, indicating the airfoil's ability to trim at positive values of angle of attack. There is also a slight decrease of moment coefficient with the increase in the angle of attack in the pre-stall regime. This suggests that the airfoil is slightly statically stable in this regime. However, it becomes statically unstable in post-stall angles of attack.

4. Profile 3 and Profile 3A

Both Profile 3 and Profile 3A possess a higher lift coefficient than other corrugated airfoils, which was observed by Kesel [16]. The 'head-on' study and comparison of Profile 3 and Profile 3A provides a closer insight into the application of corrugated airfoils for the design of MA vs. operating at a Reynolds number of around 100,000. As mentioned earlier that Profile 3A is smoothed version of Profile 3, generated by joining the extrema of the corrugated airfoil Profile 3 as done by Kesel [16]. Profile 3A shows the highest values of the lift coefficient upon the collocation of these two airfoils. Nonetheless, the lift curve is very close to Profile 3. Although Profile 3 possesses lower values of ' $c_{l, \max}$ ' as compared to Profile 3A, yet the coefficient of lift does not fall as sharply as it does with Profile 3A, and the stall angle

is slightly higher. However, the drag coefficient curve shows an entirely different story. Profile 3A has significantly lower drag coefficient values at most angles of attack when compared not only with Profile 3 but among all the other airfoils. The difference is very significant at angles of attack higher than 4° till post-stall regime. Though Profile 3A is the smoothed version of Profile 3, Profile 3 was found to perform poorly in terms of drag. This strengthens the notion proposed by Murphy [10] that the aerodynamic superiority enjoyed by corrugated airfoils seems to flip around $Re\ 100,000$. Finally, positive values of ' c_{m0} ' are observed for both Profile 3 and Profile 3A. The moment coefficient curve of Profile 3A is interesting as it is the only airfoil that shows such a sizeable decreasing trend in the values of ' c_m ' at as stall angles of attack are approached, suggesting that the airfoil is generating an increasing amount of pitching resistance before rising again in the post-stall angles of attack, indicating that the airfoil is marginally statically stable in this flight spectrum. Though the moment coefficient of Profile 3 also decreases with the angle of attack, the gradient is not negative as much as it is for Profile 3A.

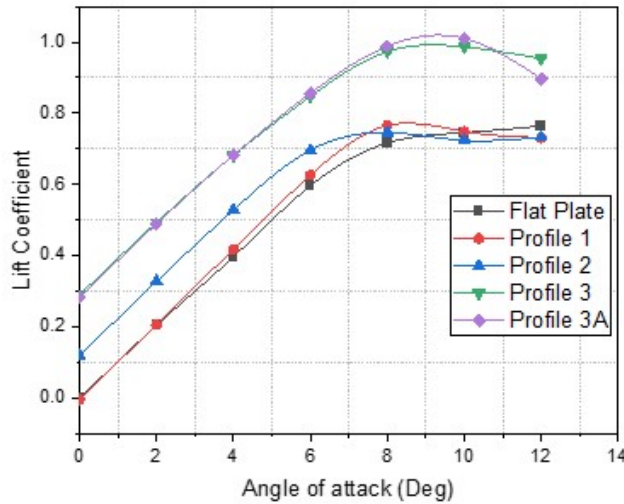


Fig. 7 C_l vs. α , $Re\ 100,000$.

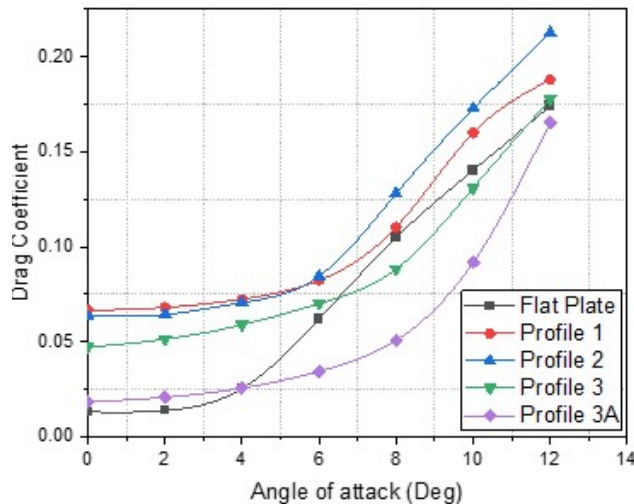


Fig. 8 C_d vs. α , $Re\ 100,000$.

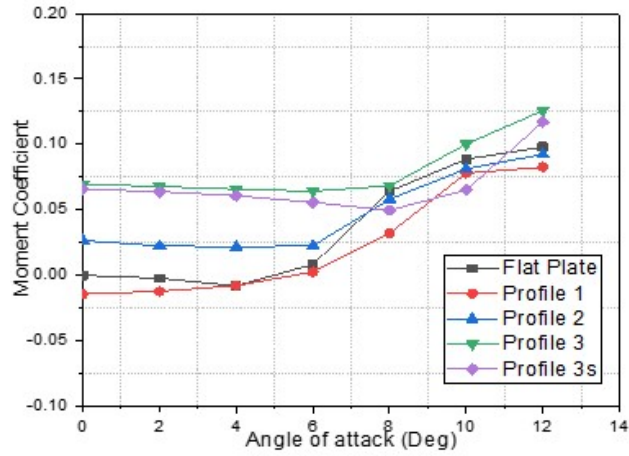


Fig. 9 C_m vs. α , $Re\ 100,000$ @ $c/4$.

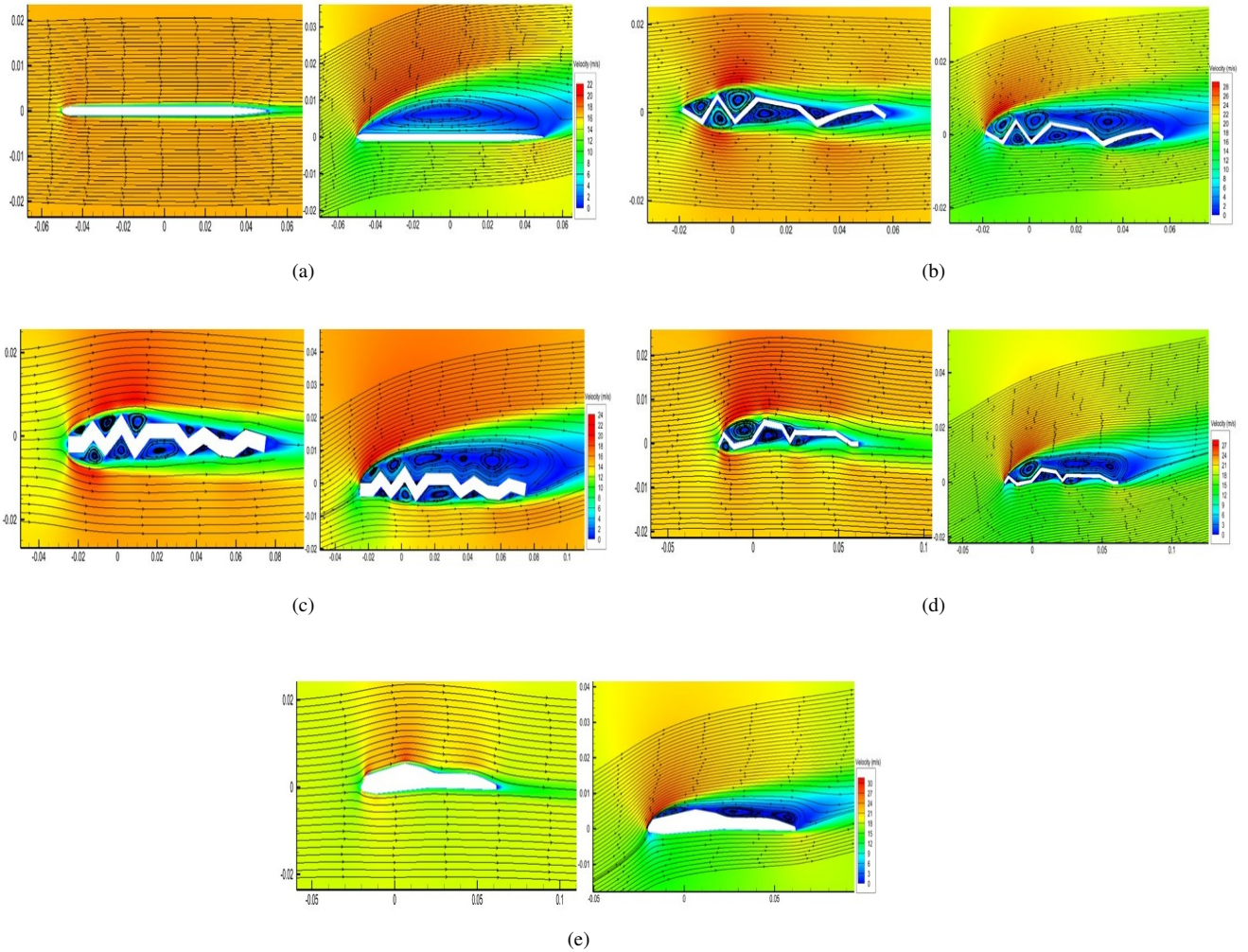


Fig. 10 Streamlines at 0° & stall angle of attack a) Flat Plate b) Profile 1 c) Profile 2 d) Profile 3 e) Profile 3A .

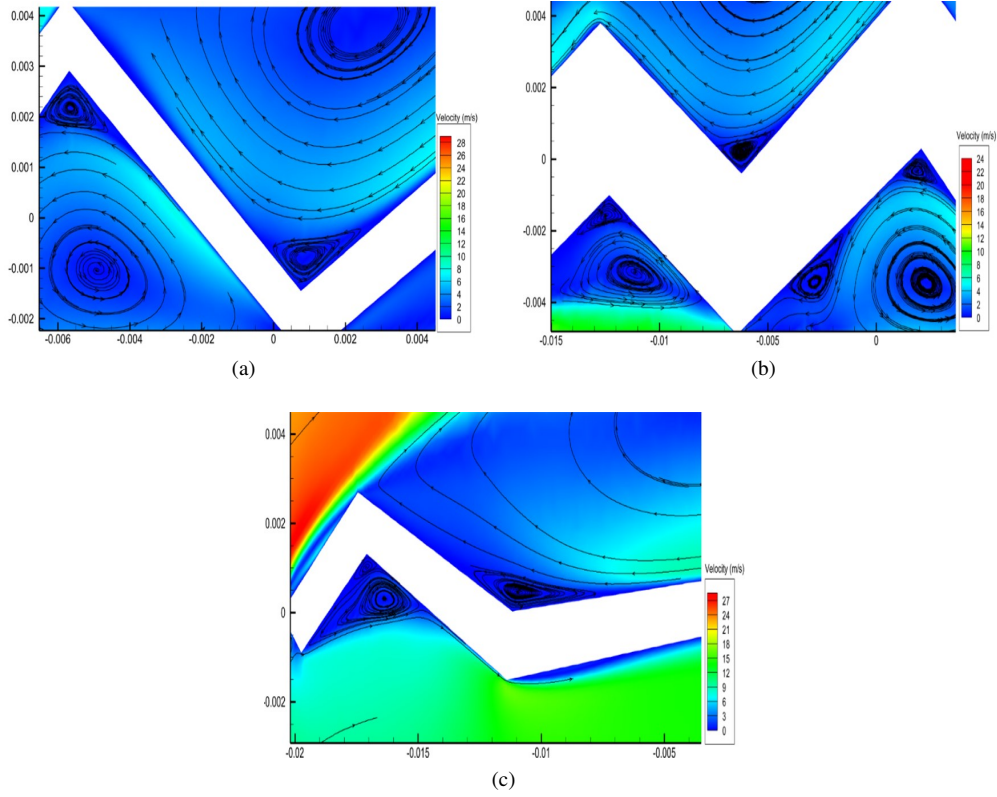


Fig. 11 Small reverse vortex region near the surface at stall a) Profile 1 b) Profile 2 c) Profile 3 .

IV. Numerical Estimation of Longitudinal Dynamic Stability Derivatives

A. Mathematical Formulation

Pitching dynamic stability derivatives can be estimated using simple formulation where pitching moment coefficient is assumed as a function of angle of attack, pitch rate and rate of change of angle of attack, and higher-order time derivatives are ignored, i.e.,

$$c_m = f_n(\alpha, q, \dot{\alpha}) \quad (1)$$

$$c_m = c_{m_0} + \frac{\partial c_m}{\partial \alpha} \alpha + \frac{\partial c_m}{\partial \bar{q}} \bar{q} + \frac{\partial c_m}{\partial \bar{\alpha}} \bar{\alpha} \quad (2)$$

After the algebraic operations and assuming linear flight conditions, Eq. 3 can be obtained from Eq. 2.

$$(c_{m_{\bar{\alpha}}} + c_{m_{\bar{q}}}) \bar{q} = c_m - (c_{m_0} + c_{m_{\alpha}} \alpha) \quad (3)$$

where ' c_{m_0} ', ' $c_{m_{\alpha}}$ ' and ' $(c_{m_{\bar{\alpha}}} + c_{m_{\bar{q}}})$ ' are defined as mean angle moment coefficient, rate of change of moment coefficient with angle of attack, moment stiffness coefficient, and damping coefficient. Also, \bar{q} and $\bar{\alpha}$ are non-dimensionalized pitch rate and rate of change of angle of attack, respectively, and are defined as

$$\bar{q} = \frac{qc}{2u_{\infty}}, \quad \bar{\alpha} = \frac{\dot{\alpha}c}{2u_{\infty}} \quad (4)$$

where ' c ' is the chord length and u_{∞} is the freestream velocity. In this method, the combined value of the damping coefficient ($c_{m_{\bar{\alpha}}} + c_{m_{\bar{q}}}$) is estimated as \bar{q} and $\bar{\alpha}$ remain equal throughout the pitch moment. These two values can be separated by introducing plunging motion to the airfoil [18, 19].

For the estimation of dynamic stability derivatives, force pitching oscillations are introduced at the quarter chord of the airfoils. By introducing these oscillations ' c_m ', ' \bar{q} ' and ' α ' becomes a function of time where ' α ' and ' \bar{q} ' is defined

as,

$$\alpha(t) = \alpha_0 + A \sin \omega t \quad (5)$$

During the pitch motion, the pitch rate and rate of the angle of attack remains the same, i.e.,

$$q(t) = \dot{\alpha} = A\omega \cos \omega t \quad (6)$$

" α_0 " represents mean angle of attack or freestream angle of attack, " ω " angular frequency, and "A" amplitude of oscillations, and these are known quantities.

Now, Reduced frequency "k", a non-dimensional parameter that determines the degree of unsteadiness in the flow is given by:

$$k = \frac{\omega \times b}{V_\infty} \quad (7)$$

where 'b' here is the mid-chord length. Angular frequency " ω " is selected in such a manner that the flow remains in a quasi-steady aerodynamic state, i.e., $k \leq 0.05$, to have a minimum phase lag and prevent the need for computationally expensive turbulence models.

CFD solver calculates the value of the coefficient of the moment at each instant of oscillation which is then plotted against the corresponding time-varying angle of attack, whose formulation is shown in Eq. 5. The obtained curve yields the parameters: mean angle moment coefficient ' c_{m_0} ' and ' c_{m_α} ' by calculating the x-intercept and curve's slope respectively using the curve-fitting method. Different curve-fitting schemes may result in different results, and it is discussed in the Amplitude Sensitivity section. Then, c_{m_0} and c_{m_α} α is subtracted from c_m at each instant of time to obtain $(c_{m_{\dot{\alpha}}} + c_{m_{\dot{q}}})\bar{q}$ as shown in Eq. (3). Finally, the obtained $(c_{m_{\dot{\alpha}}} + c_{m_{\dot{q}}})\bar{q}$ is then plotted against \bar{q} and the slope of the curve is extracted using the curve fitting method to obtain the damping coefficients, as can be seen in Eq. 8

$$\frac{\partial(c_{m_{\dot{\alpha}}} + c_{m_{\dot{q}}})\bar{q}}{\partial \bar{q}} \cong \frac{\Delta(c_{m_{\dot{\alpha}}} + c_{m_{\dot{q}}})\bar{q}}{\Delta \bar{q}} = (c_{m_{\dot{\alpha}}} + c_{m_{\dot{q}}}) \quad (8)$$

Further detail regarding the methodology for the calculation of longitudinal dynamic stability derivatives can be found in [18–20]. For the correct selection of time step size Δt in unsteady CFD simulations, time step sensitivity analysis has been done and is explained in the following section.

B. Time Step Sensitivity

In these analyses, time step size (Δt) sensitivity is carried out by keeping the product of angular velocity (ω) and time step size (Δt) as small as possible for oscillations of 1° amplitude. Increasing the angular frequency (ω) or time step size will coarsen the transient simulations and affect the accuracy of the result. Thus, it is the product of these two quantities that govern the accuracy of transient simulations. A flat plate airfoil is rotated at a zero angle of attack to carry out the time-sensitivity analyses. The frequency is kept to 1 Hz to maintain the reduced frequency less than 0.05 to remain in a quasi-steady state. This allows utilization of fewer turbulence models and to neglects the effect of phase lag. As can be seen in Fig. 12, time step size of 1/1024s appears reasonable as a slight change of 3.3% in the value dynamic stability derivatives are observed when the time step size is further reduced to half, i.e., 1/2048s while in doing so, the computation time is doubled. Time step size of 1/1024s is selected as it serves as the best available combination of computational cost and accuracy.

C. Amplitude Selection

Similarly, the effect of amplitude of the forced sinusoidal oscillations is also studied by retaining the same time step size and frequency while varying the amplitude only and plotting against damping coefficients, as shown in Fig. 14. Minor variations are observed till the amplitude of 4° . Further increment in the amplitude results in the radical change due to nonlinear effects in the pitching damping coefficients. Figure 14 also shows that choosing 1° amplitude for a given time step size is reasonable for calculating dynamic stability derivatives. Furthermore, Schmidt and Newman [18] had shown that different solutions were obtained when different curve fitting methods were used. However, a single solution was obtained when a small oscillation amplitude was selected irrespective of the curve fitting method. Because of the previously mentioned reason, an amplitude of 1° was chosen for the sinusoidal pitching oscillations.

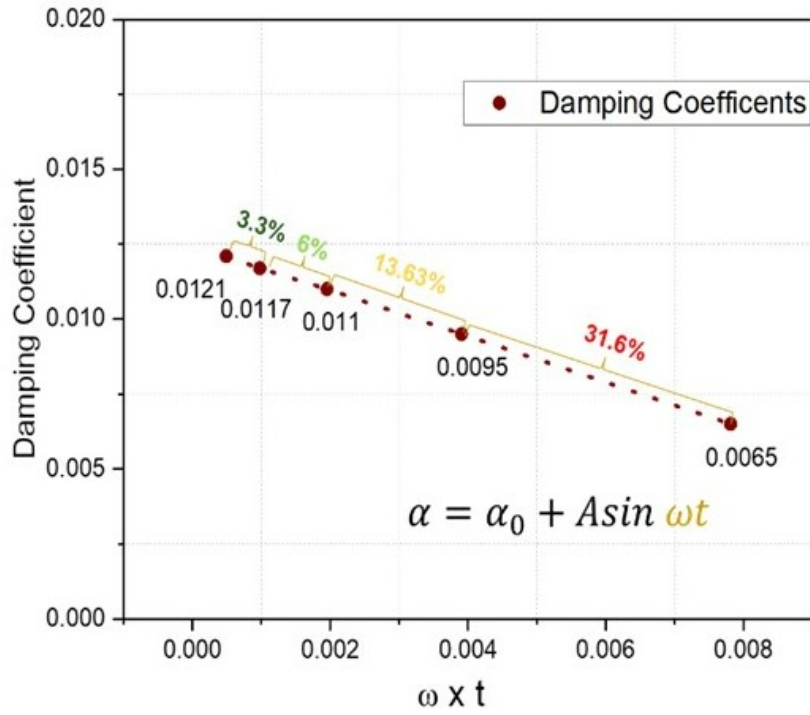


Fig. 12 Damping Coefficient vs ($\omega \times \Delta t$)

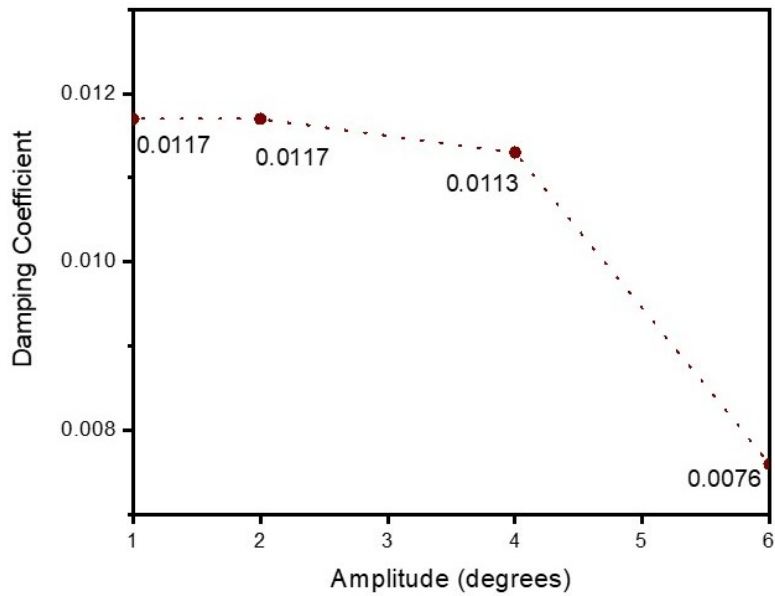


Fig. 13 Damping Coefficient vs Amplitude

D. Calculation Methodology

Pitching dynamic stability coefficients were calculated by keeping the center of gravity (CG) at the quarter-chord. The oscillations of airfoil were controlled by a user-defined function (UDF) written in C programming language and then linked with ANSYS FLUENT. However, to avoid using more complex and costly CFD models, the calculation of dynamic stability derivatives was restricted to near-stall angles of attack, i.e., till 6° . Furthermore, another set of calculations was also carried out to cater for the negative angles of attack till -6° to complete the pre-stall spectrum. All the simulations were carried out up to 5 cycles to minimize the effect of hysteresis and the error that may be induced due to the initial-developing state of the flow. As the angular frequency was 1 Hz, the simulations were performed up to 5s for each angle of attack with the time step size of 1/1024s.

The value of the moment coefficient was monitored at each time step during the airfoil's oscillations. A typically observed curve for the complete five cycles of oscillations concerning time is shown in Fig.15. The moment coefficient is then plotted vs. angle of attack to obtain the change in moment coefficient to the angle of attack in the form of a loop, which is due to the difference between moment stiffness and damping coefficients of the airfoil. Figure 16 shows such curves at a different mean angle of attack (α_0) for each airfoil. The value of c_{m_α} can be found by calculating the approximate slope of the curve using the method of least squares of the loop. The product of the terms $(c_{m_{\ddot{\alpha}}} + c_{m_{\dot{q}}})\ddot{q}$ is then computed using Eq. (3) by substituting the values of c_{m_0} and c_{m_α} to the corresponding time-varying values of moment coefficient (c_m) and angle of attack (α). Finally, the product $(c_{m_{\ddot{\alpha}}} + c_{m_{\dot{q}}})\ddot{q}$ obtained for each time step is plotted against a non-dimensionalized pitch rate (\dot{q}). As seen in Eq. 8, the slope of the curve provides an estimation of pitching dynamic stability derivatives. Figure 17 shows the value and trend of DSD of airfoils at a range of AoA from -6° to 6° .

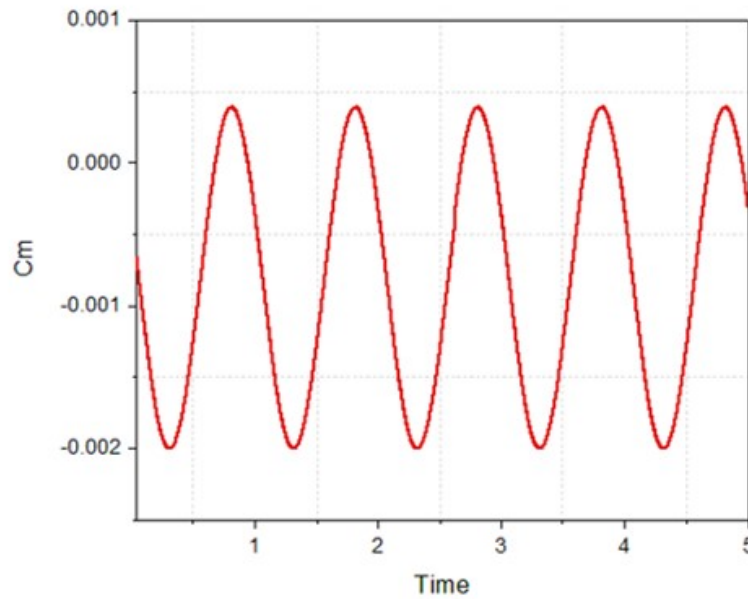


Fig. 14 Oscillation of C_m vs. time (s) at $\alpha_0=0^\circ$

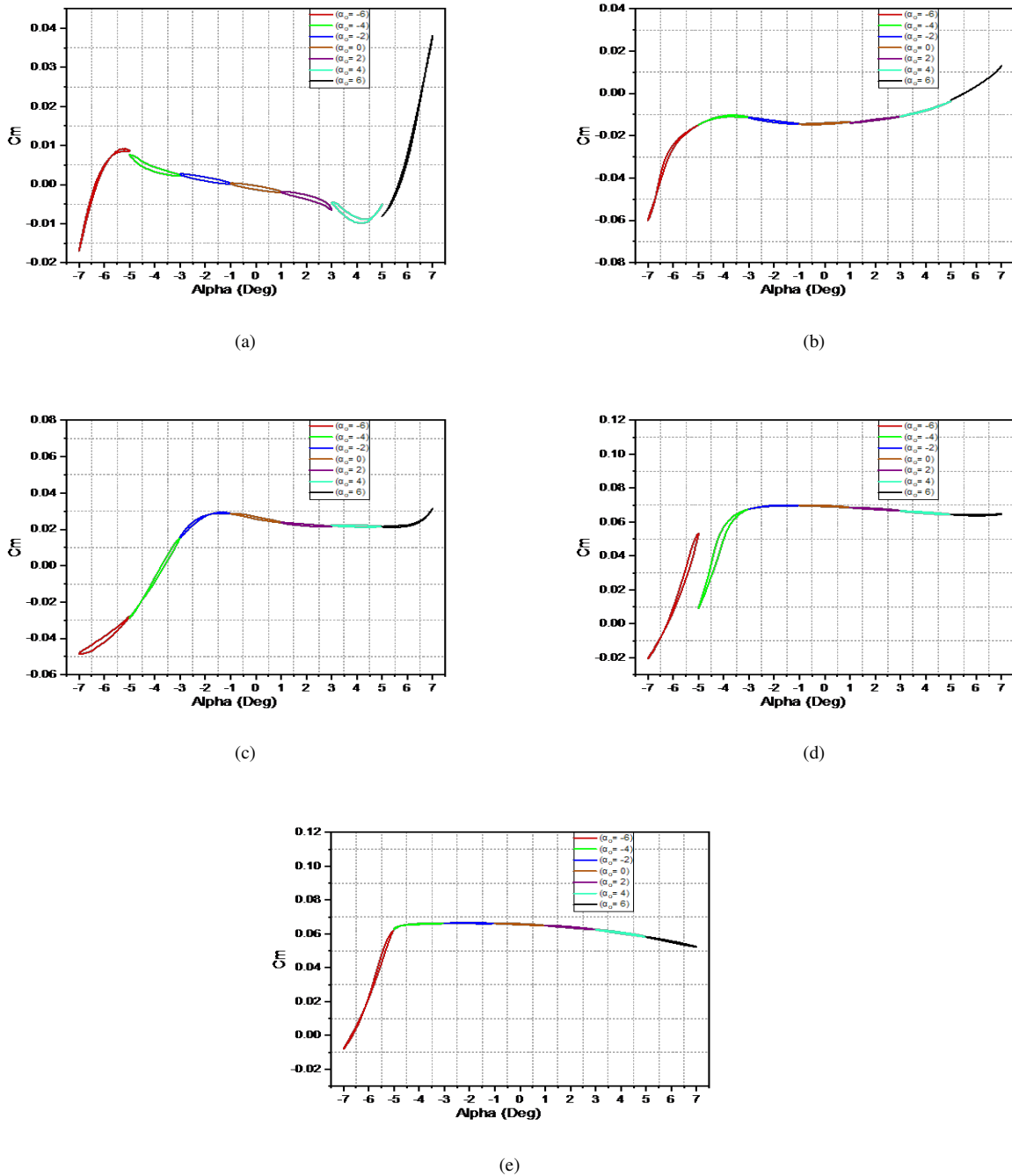


Fig. 15 Dynamic Moment Coefficient vs. Time a) Flat Plate b) Profile 1 c) Profile 2 d) Profile 3 e) Profile 3A

E. Pitching Dynamic Stability Coefficients

Longitudinal dynamic stability coefficients were calculated for each airfoil at mean angles of attack ranging from -6° to 6° with a difference of 2° . Figure 17 provides a plot of the values of stiffness coefficients and damping coefficients of airfoils at each simulated mean angle of attack. It can be seen that most of the studied airfoils are dynamically unstable at the positive angles of attack, indicating the airfoils' innate tendency to increase the disturbances over time further.

Figure 17 also shows interesting results, especially at negative angles of attack. From the 0° mean angle of attack

towards the left end, it can be seen that there is a sudden change in the values of stiffness and damping coefficients. This is due to the flow separation and reattachment and complete flow separation occurring during oscillations of the airfoils at these angles. These phenomena are nonlinear and thus increase the nonlinearity in the solution, as seen in Figure 16. The nonlinear part of the solution becomes dominant at these mean angles of attack. The same was observed at the extreme of positive mean angles of attack except for Profile 3 and Profile 3A because of their higher stall angle. The results at these angles are prone to error as a more demanding meshing, and a rigorous turbulence model was not employed to capture the trailing vortices in flow accurately. The mathematical model assumes linear flow properties. Nonetheless, the results are shown in Fig. 17 to understand the behavior of dynamic stability coefficients qualitatively.

1. Flat Plate

From Fig. 16(a), it can be seen that the variation of moment coefficient is almost linear between -4° and 4° mean angle of attack. Furthermore, the slope of the curve in this range is negative, indicating that the airfoil possesses static longitudinal stability when CG is placed at quarter-chord. This can also be confirmed from Fig. 17(a), where the airfoil has negative values of stiffness coefficients. Moreover, the stiffness coefficient was also observed to be constant around -1.5 in the linear range. However, positive values of damping coefficients in Fig. 17(b) reflect that the flat plate is dynamically unstable. The stiffness and damping coefficients are also almost symmetrical around the 0° mean angle of attack. Finally, Fig. 16(a) also shows a rapid non-linear rise in the values of moment coefficient at -6° and 6° angles. This is due to the dominance of nonlinearity in the solution due to the flow conditions. This can also be observed upon analyzing the velocity contours of the flat plate at the corresponding mean angles of attack shown in Fig 17(a). The flow is almost separated at the initial onset and becomes fully separated at -1° amplitude resulting in a low angle of attack of -7° .

2. Profile 1

Figure 16(b) also shows similar nonlinear behavior at the extreme mean angles of attack due to the reason mentioned above. The loop of the moment coefficient also remains linear in the $-4 \leq \alpha \leq 4$ AoA range. The moment coefficient vs. angle slope is positive at all mean angles of attack, suggesting that the airfoil is statically unstable, except at -2° AoA, where the airfoil is seen to have a slight negative slope showing that the airfoil is marginally statically stable as can be seen in Fig. 16(b) and Fig. 17(a). The stiffness coefficient of Profile 1 varies positively with the angle of attack, suggesting that the airfoil becomes more and more statically unstable as AoA is increased. Furthermore, Profile 1 was dynamically unstable in the range of $-4 \leq \alpha \leq 4$ angles of attack. At a 6° angle of attack, the airfoil seemed to be marginally dynamically stable yet unstable due to the positive value of the stiffness coefficient. The sharp change in the values of dynamic stability derivatives at a -6° angle of attack can be related to the flow observation shown in Fig.18(b). The fluid flow remained attached to the airfoil at the mean angle of attack before getting separated from the surface during the pitched-down motion of forced sinusoidal oscillations resulting in the observed nonlinear behavior of the results.

3. Profile 2

The moment coefficient of Profile 2 varies significantly to AoA in the range of -6° to 6° . Figure 16(c) shows that the airfoil exhibits static stability at 0° and 2° . However, beyond these angles of attack, the airfoil is statically unstable. Moreover, Profile 2 is neutrally stable at 4° . This can also be seen in Fig 17(a), as Profile 2 has near-zero stiffness coefficient values at 4° . Moreover, Profile 2 appears to be dynamically unstable at all simulated angles of attack except at -2° and -4° , at which negative damping coefficients were obtained. The abrupt change in the values of dynamic stability derivatives observed before and at -2° in Fig. 17(a-b) is again due to the flow separation during the oscillations, as seen in Fig.18(a). Another observation seen in Fig. 17 is the change in the direction of the dynamic stability curves from -4° to -6° mean angle of attack. This could be due to the complete stall state of the airfoil during the whole cycle of pitch motion, as shown in Fig. 18(a), resulting in the nonlinear behavior of the results seen in Fig. 16(c) and 17(a-b) in the span of AoA between -6° and -2° .

4. Profile 3 and Profile 3A

Similar to the aerodynamic analyses, the flight stability aspects Profile 3 and Profile 3A are also juxtaposed in this section to understand the effect of corrugations on the dynamic stability parameter. The comparison of Fig. 16(d) and Fig.16(e) shows that the magnitude of the moment coefficient of Profile 3 and Profile 3A is quite similar. From -2° to 6°

mean AoA, the slope of loop curves of both the airfoil appears to be approximately equal. This can also be observed from Fig. 17(a), where the stiffness coefficient of both airfoils is close to each other in the linear range. Both airfoils maintain marginal static instability from -2° to 2° . With the further increase in the AoA, the airfoils are slightly statically stable; especially Profile 3A is slightly more statically stable. Nonlinear behavior was observed in Profile 3 at -4° and -6° mean AoA as shown in Fig. 16(d), resulting in the sudden considerable variation of dynamic stability derivatives values shown in Fig.17(a-b). Consequently, the flow separation, reattachment, and complete stall were observed at these mean AoA depicted in Fig. 18(d) and Fig. 18(b), accounting for the nonlinear behavior. However, the flow over Profile 3A remains fully attached at -4° oscillations resulting in a linear curve shown in Fig. 16(e), Fig. 17(a-b). Flow separation and reattachment of Profile 3A were observed at -6° mean AoA. Finally, both Profile 3 and Profile 3A were found to be dynamically unstable from -2 to 6° . Moreover, there is no significant difference in the values of pitching damping coefficient between Profile 3 and Profile 3A, except in the negative angles of attack, where flow properties become highly nonlinear. This suggests that the inherent disturbance capability is insensitive to the geometrical surface protrusions and depends on the streamline ‘envelope’ the flow follows at $Re\ 100,000$.

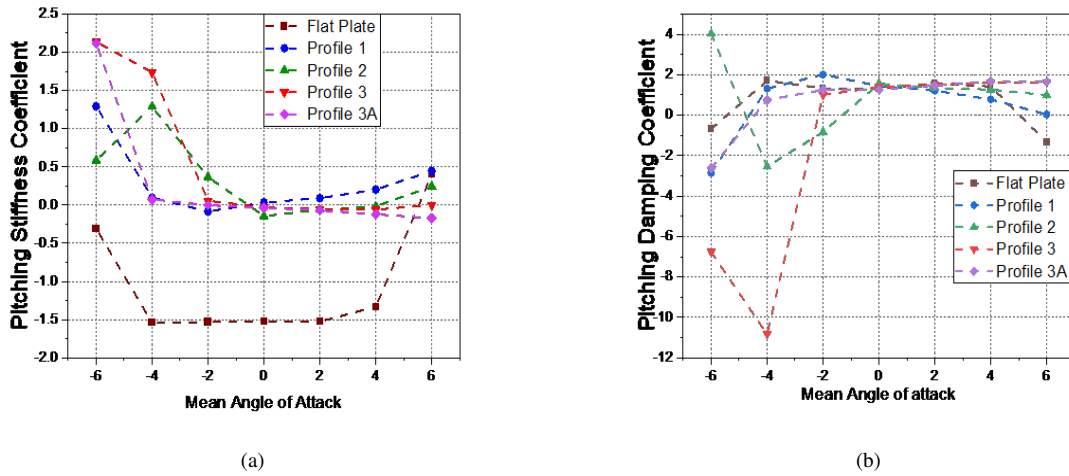


Fig. 16 Dynamic Stability Derivatives a) Stiffness Coefficient (c_{m_a}) b) Damping Coefficient ($c_{m_{\dot{\alpha}}} + c_{m_{\dot{\beta}}}$).

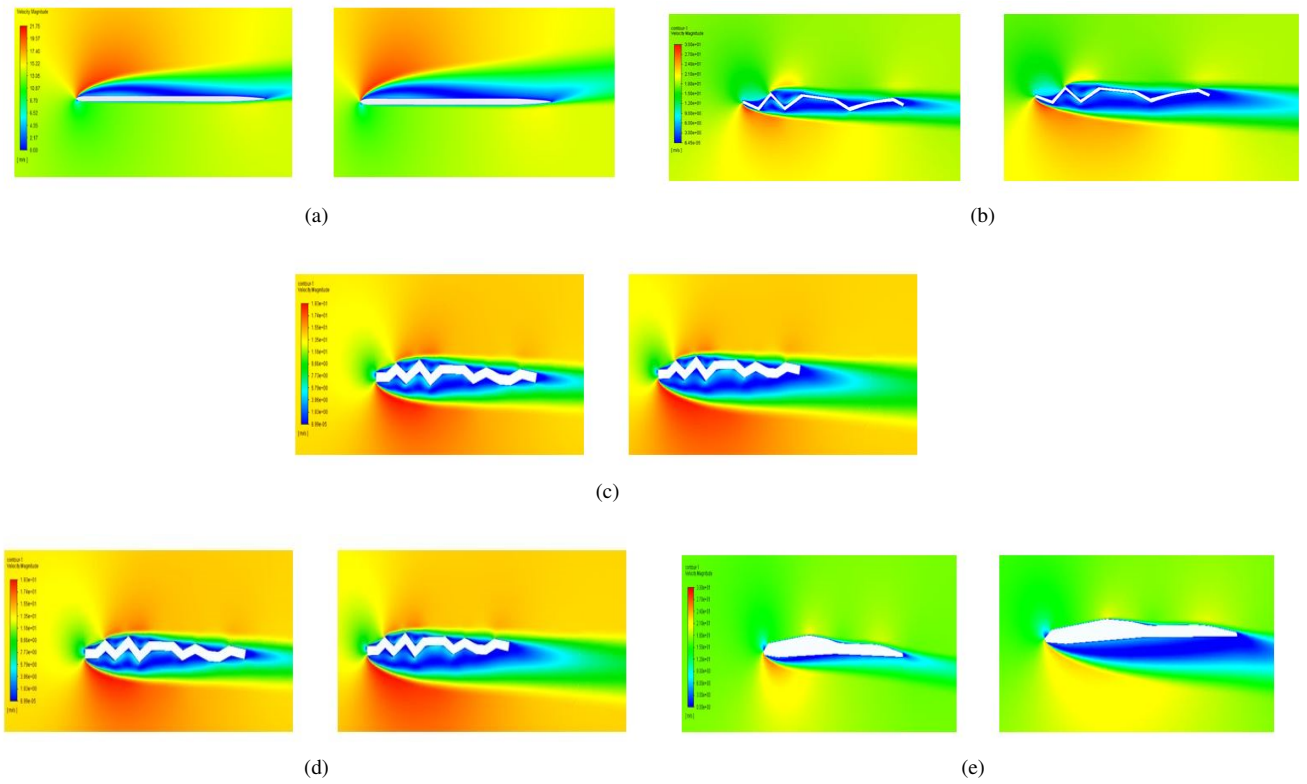


Fig. 17 Flow attached at 0° amplitude (left) and separated at -1° amplitude at corresponding mean AoA (right)
a) Flat Plate @ -6° b) Profile 1 @ -6° c) Profile 2 @ -2° d) Profile 3 @ -4° e) Profile 3A @ 6°

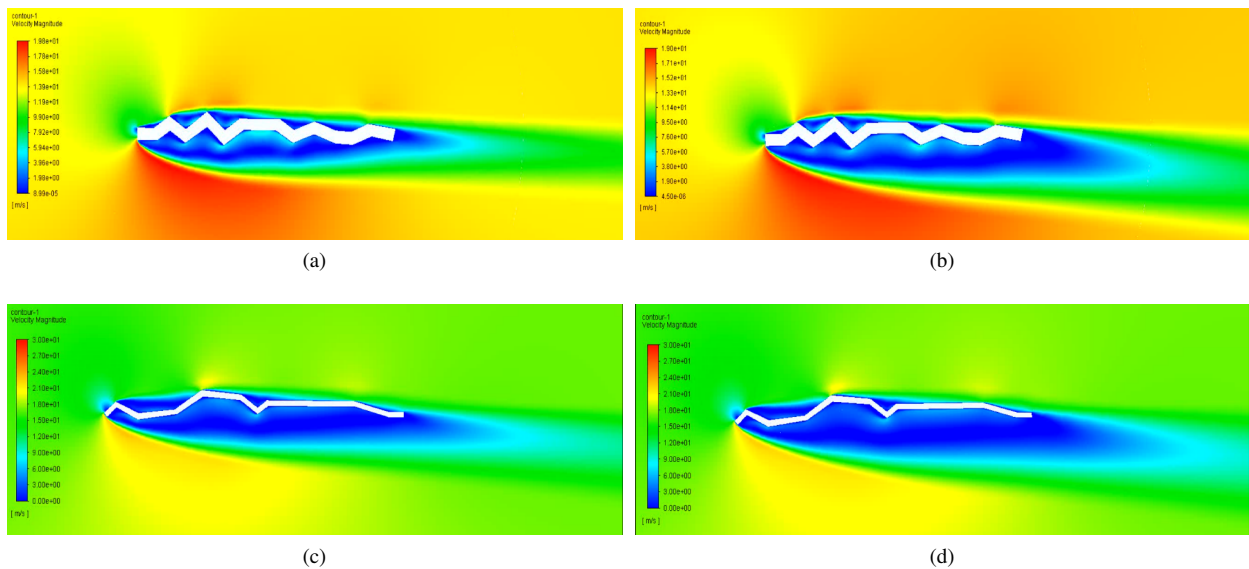


Fig. 18 Separated flow throughout at 0° and 1° amplitude at the corresponding mean AoA a,b) Profile 2 @ -6°
c,d) Profile 3 @ -6° .

V. Conclusions

In this research, aerodynamic and stability analyses were performed over five geometries of different features to explore the applicability of corrugated airfoils in the design of MAVs with the flight Reynolds number (Re) of 100,000. Spallart-Allmaras (SA) turbulence model outperformed the other Reynolds Averaged Navier Stokes (RANS), further strengthening the notion of S-A superiority over others at low Re flows.

Forced pitching sinusoidal oscillations were introduced at the quarter-chord of the airfoils to estimate dynamic stability derivatives. Time step sensitivity was performed for the CFD analyses considering the combined effect of angular frequency (ω) and time step size. The amplitude of oscillations was kept small to attain a single result from the curve fitting method. Aerodynamic and stability aspects of both pleated and smoothed airfoils were quite similar at low Re, with smoothed airfoil performing slightly better. This indicates no superiority of using corrugated airfoil in the design of MAVs that fly at Re 100,000.

Acknowledgments

The authors of this work would like to acknowledge the Computational Aeronautics Lab for providing access to the computational resources, mainly the supercomputer for performing simulations, and making a gateway for this research work to move on smoothly.

References

- [1] Pines, D., and Bohorquez, F., "Challenges Facing Future Micro-Air-Vehicle Development," *Journal of Aircraft - J AIRCRAFT*, Vol. 43, 2006, pp. 290–305. <https://doi.org/10.2514/1.4922>.
- [2] Gu, Q., Fan, T.-J., Pan, F., and Zhang, C., "A vehicle-UAV operation scheme for instant delivery," *Computers & Industrial Engineering*, Vol. 149, 2020, p. 106809. <https://doi.org/10.1016/j.cie.2020.106809>.
- [3] Albert, S., Amarilla, A., Trollope, B., Sng, J., Setoh, Y. X., Deering, N., Modhiran, N., Weng, S.-H. H., Melo, M., Hutley, N., Nandy, A., Furlong, M., Young, P., Watterson, D., Grinham, A., and Khromykh, A., "Assessing the potential of unmanned aerial vehicle spraying of aqueous ozone as an outdoor disinfectant for SARS-CoV-2," *Environmental Research*, Vol. 196, 2021, p. 110944. <https://doi.org/10.1016/j.envres.2021.110944>.
- [4] Gupta, R., Kumari, A., Tanwar, S., and Kumar, N., "Blockchain-envisioned Softwarized Multi-Swarming UAVs to Tackle COVID-19 Situations," *IEEE Network*, Vol. PP, 2020. <https://doi.org/10.1109/MNET.011.2000439>.
- [5] Gallington, R. W., Berman, H., Entzminger, J., Francis, M. S., Palmore, P., and Stratakes, J., *Unmanned aerial vehicles*, AIAA, Inc., 1997, pp. 251–295.
- [6] Anderson, J., *Fundamentals of Aerodynamics*, McGraw-Hill Education, 2005, p. 1032.
- [7] Gao, H., Hu, H., and Wang, Z., "Computational Study of Unsteady Flows around Dragonfly and Smooth Airfoils at Low Reynolds Numbers," *46th AIAA Aerospace Sciences Meeting and Exhibit*, AIAA 2008-385, 2008. <https://doi.org/10.2514/6.2008-385>.
- [8] Hu, H., and Tamai, M., "Bioinspired Corrugated Airfoil at Low Reynolds Numbers," *Journal of Aircraft*, Vol. 45, No. 6, 2008, pp. 2068–2077. <https://doi.org/10.2514/1.37173>.
- [9] Ellington, C., "The novel aerodynamics of insect flight: Applications to micro-air vehicles," *The Journal of experimental biology*, Vol. 202, 2000, pp. 3439–48.
- [10] Murphy, J., and Hu, H., "An experimental study of a bio-inspired corrugated airfoil for micro air vehicle applications," *Experiments in Fluids*, Vol. 49, 2010, pp. 531–546. <https://doi.org/10.1007/s00348-010-0826-z>.
- [11] Mazzola, A., *Low Reynolds Number Aerodynamics: Computational Study of the Aerodynamic Characteristics of a Dragonfly Aerofoil*, VDM Verlag, 2009.
- [12] RC, N., *Flight Stability and Automatic Control*, McGraw-Hill Education, 1989.
- [13] Cosyn, P., and Vierendeels, J., "Numerical Investigation of Low-Aspect-Ratio Wings at Low Reynolds Numbers," *Journal of Aircraft*, Vol. 43, 2006, pp. 713–722. <https://doi.org/10.2514/1.16991>.
- [14] Mueller, T., "Aerodynamic Measurements at Low Reynolds Numbers for Fixed Wing Micro-Air Vehicles," *Materials on the RTO AVT Course on Development and Operation of UAVs for Military and Civil Applications*, 1999, pp. 8.1–8.32.

- [15] Torres, G., and Mueller, T., "Low-Aspect-Ratio Wing Aerodynamics at Low Reynolds Numbers," *AIAA Journal*, Vol. 42, No. 5, 2004, pp. 865–873. <https://doi.org/10.2514/1.439>.
- [16] Kesel, A. B., "Aerodynamic characteristics of dragonfly wing sections compared with technical aerofoils," *Journal of experimental biology*, Vol. 203, No. 20, 2000, pp. 3125–3135.
- [17] Mueller, T. J., and Torres, G. E., "Aerodynamics of low aspect ratio wings at low Reynolds numbers with applications to micro air vehicle design and optimization," Tech. rep., Notre Dame Univ in Office of Research, 2001.
- [18] Schmidt, S., and Newman, D., "Estimation of Dynamic Stability Derivatives of a Generic Aircraft," 17th Australasian Fluid Mechanics Conference, 2010.
- [19] Rohlf, D., Schmidt, S., and Irving, J., "SACCON Stability and Control Analysis Applying System Identification Techniques," AIAA 2010-4399, 2010. <https://doi.org/10.2514/6.2010-4399>.
- [20] Greenwell, D., "Frequency Effects on Dynamic Stability Derivatives Obtained from Small-Amplitude Oscillatory Testing," *Journal of Aircraft*, Vol. 35, No. 5, 1998, pp. 776–783. <https://doi.org/10.2514/2.2369>.